Research Article | Vol. 28, No. 25 / 7 December 2020 / Optics Express 37406
Optics EXPRESS

Identifying cloud, precipitation, windshear, and turbulence by deep analysis of the power spectrum of coherent Doppler wind lidar

JINLONG YUAN,[1] HAIYUN XIA,[1,2,3,*] TIANWEN WEI,[1] LU WANG,[1] BIN YUE,[1] AND YUNBIN WU[1]

[1] *CAS Key Laboratory of Geospace Environment, School of Earth and Space Science, USTC, Hefei 230026, China*
[2] *Hefei National Laboratory for Physical Sciences at the Microscale, USTC, Hefei 230026, China*
[3] *CAS Center for Excellence in Comparative Planetology, USTC, Hefei 230026, China*
[*] *hsia@ustc.edu.cn*

Abstract: Researches on the atmospheric boundary layer (ABL) need accurate measurements with high temporal and spatial resolutions from a series of different instruments. Here, a method for identifying cloud, precipitation, windshear, and turbulence in the ABL using a single coherent Doppler wind lidar (CDWL) is proposed and demonstrated. Based on deep analysis of the power spectrum of the backscattering signal, multiple lidar products, such as carrier-to-noise (CNR), spectrum width, spectrum skewness, turbulent kinetic energy dissipation rate (TKEDR), and shear intensity are derived for weather identification. Firstly, the cloud is extracted by Haar wavelet covariance transform (HWCT) algorithm based on the CNR after range correction. Secondly, since the spectrum broadening may be due to turbulence, windshear or precipitation, the spectrum skewness is introduced to distinguish the precipitation from two other conditions. Whereas wind velocity is obtained by single peak fitting in clear weather condition, the double-peak fitting is used to retrieve wind and rainfall velocities simultaneously in the precipitation condition. Thirdly, judging from shear intensity and TKEDR, turbulence and windshear are classified. As a double check, the temporal continuity is used. Stable wind variances conditions such as low-level jets are identified as windshear, while arbitrary wind variances conditions are categorized as turbulence. In the field experiment, the method is implemented on a micro-pulse CDWL to provide meteorological services for the 70th anniversary of the China's National Day, in Inner Mongolia, China (43°54′N, 115°58′E). All weather conditions are successfully classified. By comparing lidar results to that of microwave radiometer (MWR), the spectrum skewness is found be more accurate to indicate precipitation than spectrum width or vertical speed. Finally, the parameter relationships and distributions are analyzed statistically in different weather conditions.

1. Introduction

The atmospheric boundary layer (ABL) plays an important role in many fields, including air pollution and the dispersal of pollutants, agricultural meteorology, aeronautical meteorology, mesoscale meteorology, and weather forecasting [1]. Accurate weather condition measurement and classification with high temporal and spatial resolutions are essential not only for engineering applications, but also for scientific research. For example, windshear and severe turbulence will cause aircraft loss of control and deviate from the intended flight path [2], and freezing precipitation may deteriorate the aircraft's aerodynamic performance [3]. To understand the microphysical process of the ABL, one needs knowledge of transport and mixing conditions including wind profiles, turbulence, windshear, precipitation, and cloud [4].

Numerous instruments have been applied to study the characteristics of the ABL. Airborne sensors [5,6], space-borne sensors [7,8], and ground-based remote sensing measurements such

#412809 https://doi.org/10.1364/OE.412809
Journal © 2020 Received 19 Oct 2020; revised 14 Nov 2020; accepted 17 Nov 2020; published 24 Nov 2020

Optics EXPRESS

as sodars [9,10], radars [11,12], microwave radiometers [13–15] and lidars [16–20] are widely used in recent decades. Among these instruments, lidars can make measurements alone with multiple scanning mode, high temporal and spatial resolutions, and high accuracy.

The CDWL has been used in some precipitation detection scenarios based on the power spectrum [21,22]. The common criterion for identifying rainfall is the spectrum broadening phenomenon, due to the velocity difference between rain drops and aerosol. This method is only valid for rain condition when the power spectrum shows two-peak structure clearly. However, it hard to recognize all rain conditions by spectrum broadening effect, such as drizzle or in the condition when aerosol is nearly washed out by the rain. In such cases, since one spectrum is dominated, the weaker one is submerged. Besides, other meteorological features can also lead to spectrum broadening, including windshear, turbulence, and multiple scattering of clouds [23–26].

Turbulence measurements using ground-based wind lidars are reviewed in [27]. Various parameters are used to estimate turbulence quantity using a lidar, including turbulent kinetic energy dissipation rate (TKEDR), radial velocity variance, coherence of the components of the wind field, etc. Compared with stable windshear, turbulence is caused by rapid irregular motion of air. Therefore, the distribution characteristics of wind variation provide an opportunity to distinguish turbulence and windshear.

In this work, a method using a single CDWL is proposed to detect and identify cloud, precipitation, windshear, and turbulence by deep analysis of power spectrum, to provide meteorological services for the 70th anniversary of the China's National Day. The sites, instruments are described in Sect. 2. Sect. 3 introduces the lidar products derived from power spectrum. In Sect. 4, observation, identification, and statistical results are present. Finally, a conclusion is drawn in Sect. 5. If not specified, local time is used.

2. Site and instruments

The field experiment is performed at Xilin Gol grassland, Inner Mongolia, China (43°54′N, 115°58′E), from 28 August to 1 October 2019. The site is in the hinterland of Xilingol grassland, with a typical temperate continental climate. Due to the frequent invasion of polar dry and cold air, the site is usually windy weather in autumn.

2.1. Coherent Doppler wind lidar

A compact and integrated micro-pulse CDWL with high temporal and spatial resolutions is applied. The CDWL is shown in Fig. 1. It can work continuously in different weather conditions with an all-fiber structure and temperature control system. The CDWL is operated at an eye-safe wavelength of 1.5 μm. The pulse energy of the laser is 100 μJ. The key parameters are listed in Table 1. The CDWL supports multiple scanning modes, including plan position indicator (PPI), range height indicator (RHI) and velocity azimuth display (VAD). The reliability of the CDWL is demonstrated in previous works. [22,28,29]

Fig. 1. Photograph of the CDWL and microwave radiometer in the airport.

Optics EXPRESS

Table 1. Key Parameters of the CDWL

Parameter	Value
Wavelength	1548 nm
Pulse Energy	100 μJ
Repetition frequency	10 kHz
Accumulated pulse number	10000
Diameter of telescope	80 mm
Temporal resolution	2 s
Maximum range	15 km
Azimuth scanning range	0 - 360°
Zenith scanning range	0 - 90°

During the experiment, the lidar operates in the VAD scanning mode with a period of 2.5 min. The elevation angle is fixed at 60°. The azimuth angle changes from 0° to 300°, with a stepping angle of 5°. The radial spatial resolutions are set as 30/60/150 m in the range of 0-2.5/2.5-5.5/5.5-13.0 km. The resolution change is used to improve the detection probability in the high altitude where the aerosol concentration is usually low. Velocity components are retrieved by the filtered sine wave fitting (FSWF) method with radial wind velocities [30].

2.2. Microwave radiometer

A ground-based microwave radiometer (MWR) is used in the experiment, as shown in Fig. 1. The MWR provides atmospheric profiles of temperature, water-vapour, liquid water, and relative humidity, from the surface to a height of 10 km. The vertical resolutions are set as 50/100/250 m in the height of 0-0.5/0.5-2/2-10 km. The temporal resolution is 2 min. Application and detail specifications of the MWR are demonstrated in [31].

3. Principle

3.1. Characteristics of the power spectrum

The line of sight (LOS) velocity is determined by the mean Doppler frequency shift of the power spectrum. The sign is defined as positive when the movement is toward the lidar, and vice versa. The carrier-to-noise ratio (CNR) is the ratio of signal power to noise power. The accuracy of velocity estimation is mainly determined by the CNR [20,32]. The signal spectrum width is an indicator of velocity dispersion in a range bin. Adverse weather conditions can result spectrum broadening, such as windshear, turbulence, and precipitation. Besides the CNR and spectrum width, skewness is introduced to reveal how adverse weather conditions affect the power spectrum in this work. Skewness is a measure of the symmetry of the power spectrum. The skewness is expressed as:

$$Sk = \frac{\sum (v_i - \bar{v})^3 P_i}{\sum P_i} \Big/ \left[\frac{\sum (v_i - \bar{v})^2 P_i}{\sum P_i} \right]^{1.5} - Sk_0 \tag{1}$$

where v_i and P_i are the velocity and power spectrum value at sampling point i, respectively. $\bar{v}$ is the mean velocity. The negative skewness means that the spectrum is a left bias curve, and vice versa. In general, the spectrum has a single peak distribution with a small skewness of Sk_0 near to zero, because the shape of emitted pulse is not strictly Gaussian. Sk_0 can be estimated from spectra in clear air conditions with weak turbulence and windshear. Sk is not effective to identify the multi-peak structure. For example, Sk is close to zero for the spectrum having two similar intensity peaks in some precipitation conditions. Therefore, the skewness is modified in Eq. (1). $\bar{v}$ is set as the velocity associated with the maximum of signal intensity.

Optics EXPRESS

3.2. Calculation of turbulence and shear intensity

The TKEDR is a method for turbulence measurements using ground-based wind lidars [27]. The greatest advantage of estimation of TKEDR is that the universal behaviour of isotropy in the inertial subrange is used, either in the Fourier domain (using velocity spectrum) or in the temporal domain (using structure function). In this work, a method of azimuth structure function is applied to estimate the TKEDR in the VAD scanning mode. The method including error analysis are demonstrated in detail [18,33].

Windshear is the vector difference between the winds at two points. The shear intensity is calculated by dividing the magnitude of the vector difference between the two points by the distance, i.e. the velocity gradient of wind profiles [2]:

$$\overrightarrow{Sh} = (\partial u_i/\partial z_i, \partial v_i/\partial z_i) \tag{2}$$

where u_i and v_i are wind components at height z_i, the shear intensity modulus of wind profiles has random fluctuations, due to the atmosphere turbulence.

3.3. Cloud extraction

The Haar wavelet covariance transform (HWCT) method is used to retrieve boundary layer height (BLH) from aerosol concentration [34]. The HWCT method is less affected by signal noise, with good adjustability and robustness. Here, the HWCT method is adopted to extract the cloud based on CNR after range correction, which reflects the aerosol concentration. Clouds are characterized by a steep increase of the range corrected lidar signal at the cloud base followed by a strong decrease of the signal at the cloud top. The determination of the cloud base and top is discussed in details [35,36].

4. Observations, identification, and analysis

4.1. Preliminary observations

Figure 2 shows continuous CDWL observation results of low-level jets and turbulence during 27-28 September 2019. The receiver bandwidth is 125 MHz, for CNR calculation. Since the detection probability in the high altitude is improved at sacrifice of range resolution as mentioned in section 2.1, the CNR increases above 2.2 km, as shown in Fig. 2(a). Therefore, the CNR is range corrected for cloud extraction. The spectrum width is shown in Fig. 2(b). Both turbulence and windshear can cause the velocity of aerosol to deviate from the mean value, resulting in spectrum broadenings. However, the value of skewness does not increase obviously, as shown in Fig. 2(c). The skewness is corrected by Eq. (1), and the estimated Sk_0 is 0.02. Low-level jet is detected during the night and early morning. The low-level jet altitude is identified using the method presented by [37], as shown both in Fig. 2(d) and (e). The surface turbulence is generated by the drag of the low-level jet, the TKEDR is shown in Fig. 2(g). However, the low-level jet is interrupted by the turbulence generated by solar heating during the day time [38]. Because turbulent motion is enhanced by updraft from the ground, due to the solar radiation enhancing. Convection characteristics of vertical velocity also characterize turbulence, as shown in Fig. 2(f). The cloud attenuates the solar radiation sometimes during the daytime, decreasing the updraft. Consequently, the turbulence is weakened, as shown in Fig. 2(g). The error of radial velocity should be smaller than 0.5 m/s for wind vector estimation by FSWF method [39], thus the data with CNR below -35 dB are abandoned [20,29]. Higher quality data is needed for TKEDR estimation [33,40]. The CNR criterion is set to -27 dB for TKEDR, where radial velocity error the CDWL is not exceeding 0.2 m/s [20]. Hence the retrieval possibility of TKEDR is below than that of shear intensity, as shown in Fig. 2(h). Low-level jet cases identified in Fig. 2(d) and (e) can estimate the max velocity position in the low-level jet, while the shear intensity can reflect the

Optics EXPRESS

windshear intensity in temporal and spatial ranges. The shear intensity driven by turbulence is disorderly, while that of low-level jet is zonal in the time axis. Stable windshear such as low-level jet has the features of temporal continuity. Here, this phenomenon is selected as a criterion for distinguishing windshear from turbulence.

Continuous observation results including four precipitation cases are obtained by the CDWL from 28 August to 1 October 2019, as appended in the dataset [41]. Figure 3 shows a precipitation process, during 19-20 September 2019. At 19 September, 0:00, clouds at the height of 7 km start sinking with a vertical speed about 1 m s-1, as shown in Fig. 3(f). The skewness deviates significantly from zeros, from 23:00 on 19 September to 5:30 the next day, a total of 6.5 hours, as shown in Fig. 3(c). In the meantime, the spectrum width is broadened obviously, as shown in Fig. 3(b), and large sinking speeds are observed, as shown in Fig. 3(f). Apparently, the precipitation occurred during this period. The skewness increasing indicates that multiple components exist in the power spectrum of precipitation, due to the different velocities of aerosol and raindrop. Comparing to the spectrum width or vertical speed, the skewness provides a more accurate criterion to distinguish precipitation from windshear and turbulence. The temperature, water-vapour, liquid water, and relative humidity observed by MRR are shown in Fig. 4. In the early stage of rainfall, the liquid water is below 0.1g m^{-3}, and the water-vapour is above 6 g m^{-3}, below 2 km. The raindrops are evaporated due to arid conditions, increasing water-vapour. After a period of rainfall, the water-vapour, liquid water, and relative humidity increase significantly. The MWR results are consistent with that of the lidar.

4.2. Identification procedure and results

An identification procedure of cloud, precipitation, windshear, and turbulence is introduced in this section. It incorporates the following lidar productions derived from the deep analysis of the power spectrum: CNR, spectrum width and skewness of power spectrum, TKEDR, and shear

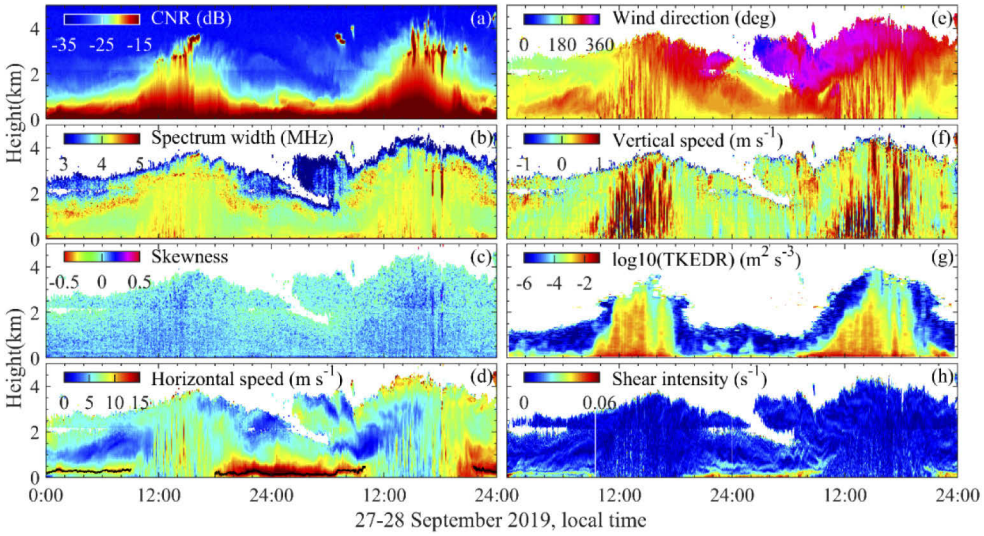

Fig. 2. Continuous CDWL observations of low-level jets and turbulence during 27-28 September 2019. (a) CNR, (b) spectrum width, (c) skewness, (d) horizontal wind speed, (e) horizontal wind direction, (f) vertical wind speed, (g) log10(TKEDR), (h) shear intensity. The negative vertical wind speed indicates upward wind. The black lines on (d) and (e) show low-level jet altitude identified using the method presented by [37].

Optics EXPRESS

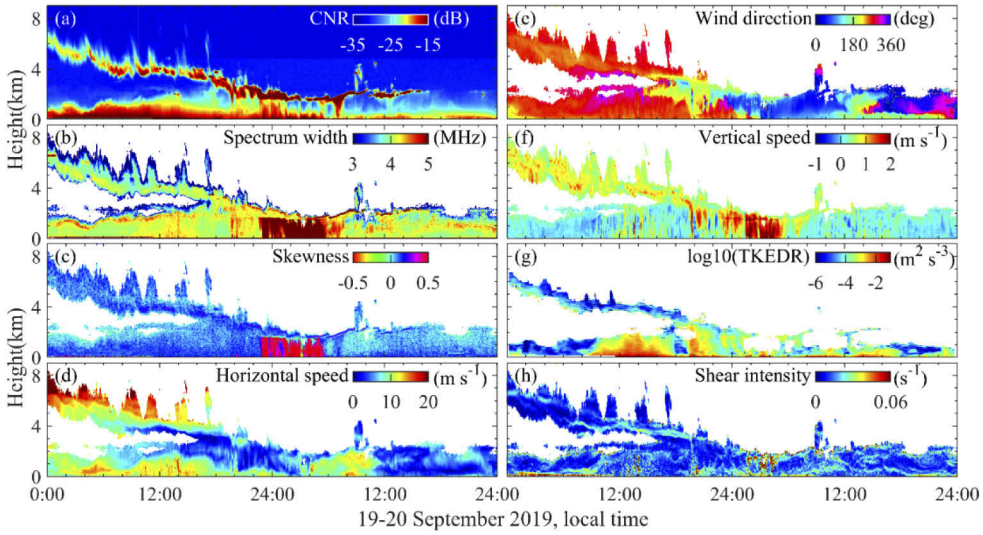

Fig. 3. A precipitation process observed by the CDWL during 19-20 September 2019. (a) CNR, (b) spectrum width, (c) skewness, (d) horizontal wind speed, (e) Horizontal wind direction, (f) vertical wind speed, (g) log10(TKEDR), (h) shear intensity.

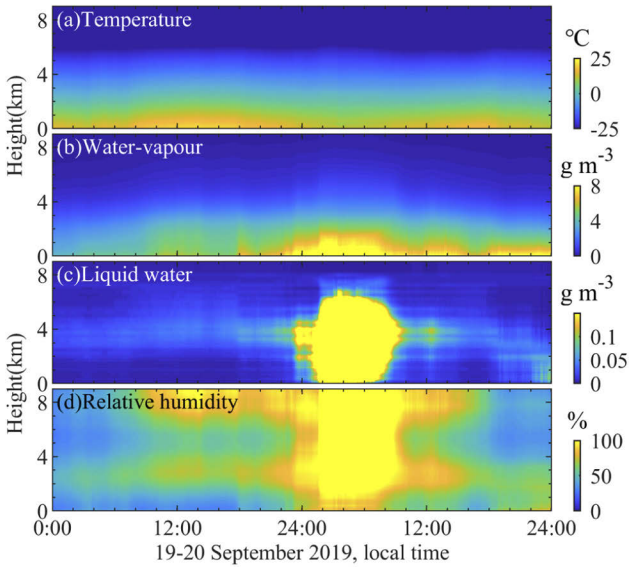

Fig. 4. Continuous MWR observation results during 19-20 September 2019.

Optics EXPRESS

intensity, as introduced in Sect. 3. Figure 5 is the flowchart of the identification procedure, as described below:

1. Firstly, the power spectrum is obtained from the CDWL raw data by using fast Fourier transform. And the CNR, spectrum width, and skewness are derived from the power spectrum.

2. Then, the cloud is extracted by CNR after range correction, using the HWCT method.

3. Except the method based on spectrum width, in previous works, precipitation cases are identified by the vertical velocity data using the assumption that all precipitations have a fall velocity greater than a threshold. The threshold is set as >1 m s^{-1} [19] and >1.5 m s^{-1} [15], respectively. Since precipitation is more coherent in the vertical dimension, using suitable time and vertical windows can obtain a robust result. However, could motion, large-scale vertical motion arising from orographic features or strong convection such as microburst can also cause a vertical velocity, which may introduce false precipitation identification. To improve the identification accuracy and capture the detail of precipitation features, skewness is introduced in addition to the spectrum broadening to identity the precipitation. The thresholds of spectrum width and skewness can be obtained, according to the precipitation results from Fig. 3, which are confirmed by MWR. The empirical thresholds of spectrum width and skewness are recommended to be >4.5 MHz and >0.2, respectively. After the identification of the precipitation spectrum, rain and wind velocity are simultaneously retrieved by double-peak fitting, as demonstrated in [21,22,29].

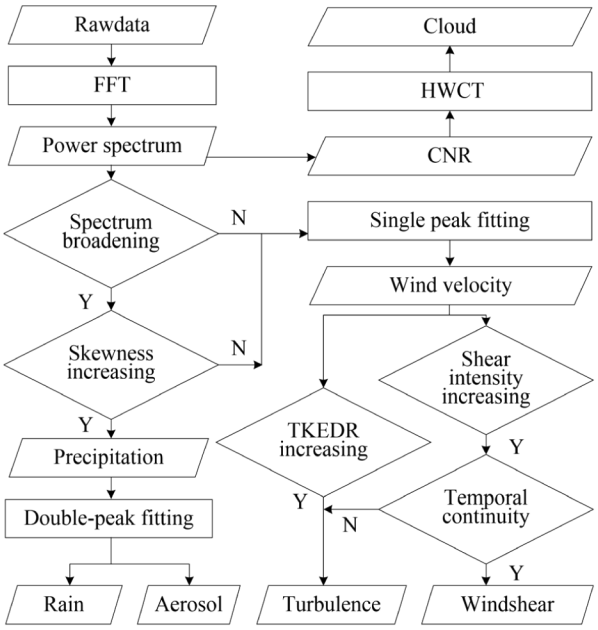

Fig. 5. The identification procedure of cloud, precipitation, turbulence, and wind shear in a VAD scanning.

Figure 6 shows examples of the Doppler spectrum in precipitation conditions. The aerosol and rain spectra are obtained using double-peak fitting. The right spectrum is tagged as the rain signal, as discussed elsewhere [22]. Figure 6(a) and (b) show the spectrum with obvious double-peak distribution. The aerosol component dominates with positive skewness in Fig. 6(a), while the rain component dominates with negative skewness in

Optics EXPRESS

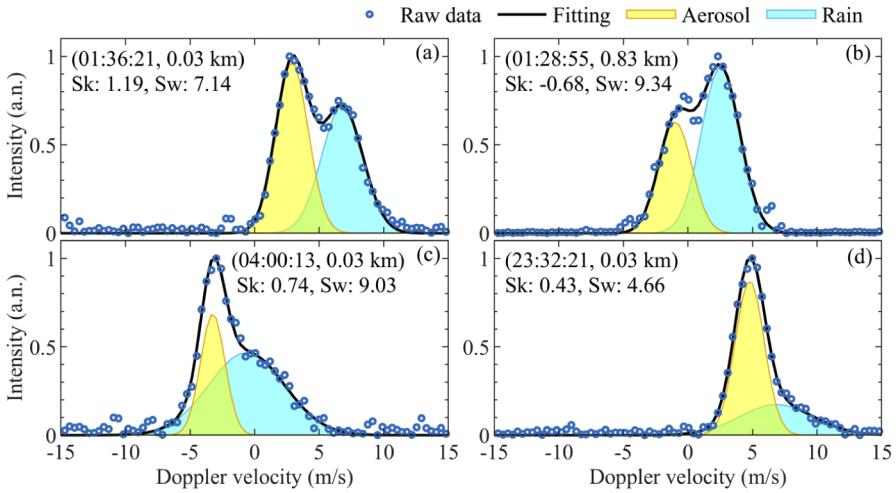

Fig. 6. Examples of the Doppler spectrum in precipitation conditions from 23:00 on 19 September to 5:30 the next day. (a) and (b) show obvious double-peak distribution spectra. (c) and (d) show spectra that the rain spectra are covered by that of aerosol. The *Sw* and *Sk* are the spectrum width and skewness of the raw spectrum.

Fig. 6(b). Figure 6(c) and (d) show cases where the rain spectra are covered by aerosol ones. The spectrum width broadening of the raw spectrum in Fig. 6(d) is not obvious, compared with these of (a), (b), and (c), while the spectrum skewness reaches to 0.43, demonstrating the effectiveness of this method.

4. After recognizing of cloud and precipitation, the windshear and turbulence are identified by a threshold approach based on TKEDR and shear intensity. The turbulence is obtained with the TKEDR threshold $>10^{-4}$ $m^2 \cdot s^{-3}$, recommended in previous studies [42–44]. To expand the search band for turbulence, the irregular windshear is classified as turbulence, which could be wind-shear derived or cloud derived turbulence. The windshear region is

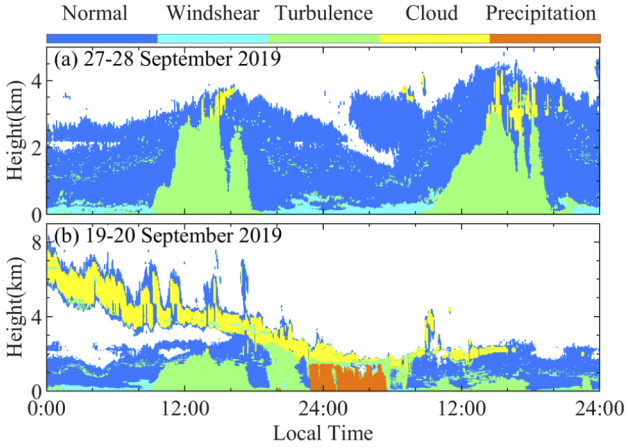

Fig. 7. The identification results of (a) 27-28 September 2019, and (b) 19-20 September 2019.

Optics EXPRESS

identified when shear intensity is greater than 0.02 s^{-1} [4]. A time window recommend as 36 min is applied to filter the irregular windshear.

Figure 7 shows the identification results of 27-28 September 2019 and 19-20 September 2019. The LOS velocity used to determine the velocity vector in Fig. 2 and Fig. 3, are obtained by one peak fitting. It is inaccurate for precipitation condition, since both aerosol and rain spectra exist. In precipitation, double-peak fitting is applied to separate the aerosol and rain components in the power spectrum. The separation results of wind and rain are shown in Fig. 8. The rain spectrum width is wider than that of aerosol as shown in Fig. 8(a) and (e). The spectrum width of aerosol in Fig. 8(a) is broadened during the precipitation, due to wind variances. The horizontal speed and direction of raindrops are close to that of wind, as shown in Fig. 8(b), (c), (f), and (j). It is caused by the drag effect of wind on raindrops in horizontal direction. Raindrops are obviously heavier than aerosol particles, thus the vertical speeds of raindrops are larger than that of wind, as shown in Fig. 8(d) and (h). The vertical speed of raindrops reflects the raindrop size [21]. Heavy rain is often accompanied by big raindrops that have large falling speed, while light rain usually consists of small drops.

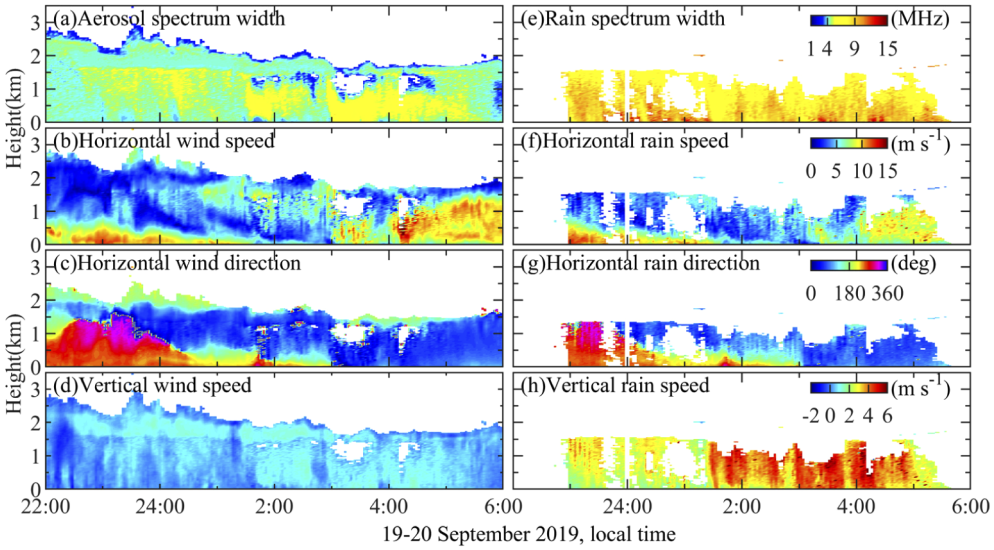

Fig. 8. Separation results of wind and rain. (a) Aerosol spectrum width; (b) Horizontal wind speed; (c) Horizontal wind direction; (d) Vertical wind speed. (e) Rain spectrum width; (f) Horizontal rain speed; (g) Horizontal rain direction; (h) Vertical rain speed.

To analyse the characteristics of the identification results in Fig. 7, the parameter relationships are drawn in Fig. 9. The shear intensity, spectrum width, spectrum skewness, and vertical speed are selected. It should be specified that the shear intensity, spectrum width, and vertical speed of the precipitation are updated by two-peak fittings. The distribution centres of the precipitation, windshear and turbulence are marked as white inverted triangle, black circle, and white square. The detailed values are listed in Table 2. Two precipitation clusters are shown in Fig. 9(a), (c), and (e). The right precipitation cluster with positive skewness represents cases that the aerosol component dominates. The left precipitation cluster with negative skewness represents cases that the rain component dominates. The skewness centres of precipitation clusters are -0.474 and 0.445, respectively. The spectrum width and vertical centres of precipitation are 8.413 MHz, and 3.367 m s^{-1}, significantly greater than that of windshear and turbulence. Combining the spectrum width and skewness, it is easy to identify precipitation from windshear and turbulence, as shown in Fig. 9(c). Strong shear intensity exists in precipitation, as shown in Fig. 9(a), (b), and

Optics EXPRESS

(f), because significant changes in wind direction and velocity are often happened, as examples shown in Fig. 8(b) and (c). From Fig. 9(c), (d), and (e), it is hard to distinguish windshear from turbulence using the spectrum width, spectrum skewness, and vertical speed, since the distribution centres of them almost coincide. Nevertheless, the distribution of the shear intensity is obviously different, as shown in Fig. 9(a), (b), and (f). The shear intensity centre of 0.03 s^{-1} is obvious greater than 0.008 s^{-1} that of turbulence.

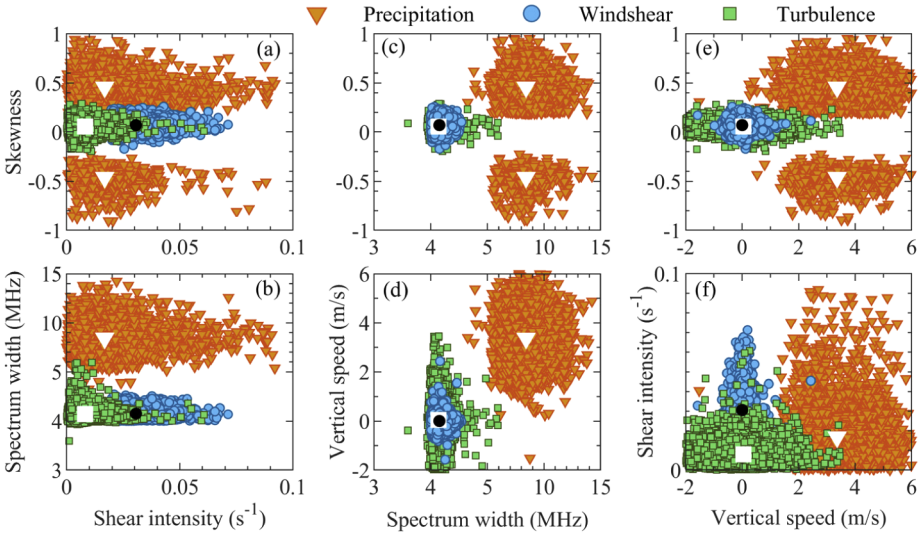

Fig. 9. Parameter relationship of precipitation, windshear, and turbulence. Shear intensity with (a) skewness and (b) spectrum width. Spectrum width with (c) skewness and (d) vertical speed. Vertical speed with (e) skewness and (f) shear intensity. The inverted triangle, circle, and square represent the precipitation, windshear, and turbulence.

Table 2. Classification centres

Parameter	Normal	Turbulence	Windshear	Precipitation
Skewness	0	0.054	0.072	**-0.474**, **0.445**
Spectrum width (MHz)	3.843	4.143	4.152	**8.413**
Shear intensity (s-1)	0.007	0.008	**0.031**	0.017
Vertical Speed (m s-1)	-0.003	0.051	0.001	**3.367**

The probability density function (PDF) of parameters is estimated using the kernel density estimation (KDE), as shown in Fig. 10. The area of red shade in Fig. 10(a) is 98.9%, which reflects the identification rate for precipitation using the skewness threshold of 0.2. The spectrum width PDF of precipitation is a normal distribution, which is distinguished from that of windshear and turbulence, as shown in Fig. 10(b). From Fig. 10(c), the shear intensity PDF of windshear is distinct from that of turbulence. There exists an overlap between shear intensity PDF of windshear and precipitation, but the precipitation has been identified before windshear and turbulence, verifying rationality of the identification procedure. The PDFs of vertical speed are normal distribution, as shown in Fig. 10(d). Since the turbulence is accompanied with vertical air motion, the vertical velocity distribution of turbulence varies more widely than that of windshear.

Optics EXPRESS

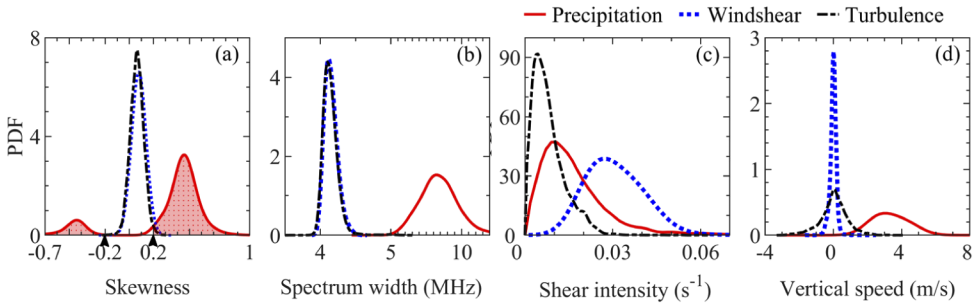

Fig. 10. The PDF estimated by using the kernel smoothing estimation. (a) Skewness, (b) Spectrum width, (c) Shear intensity, (d) Vertical speed.

5. Conclusion

A method for weather identification is introduced based on several CDWL products derived from the power spectrum. The method is verified on a field experiment, all mentioned weather conditions are successfully detected and identified. The spectrum skewness introduced in this work can indicates precipitation accurately. It reflects the difference in doppler shift of aerosol and precipitation particles, including cases where the weaker spectrum is submerged in the other one. The estimated recognition rate of precipitation using the skewness threshold of 0.2 is 98.9%. The skewness threshold can be updated by iteration to improve the identification rate, because the threshold may vary for different CDWLs or sites. Statistical results show that the precipitation is accompanied with strong shear intensity and large vertical speed. Therefore, it is important to identify precipitation before windshear and turbulence. After that, stable windshear can be distinguished from turbulence, since windshear is persistent in time with strong shear intensity. In summary, by deep analysis of the power spectrum of CDWL, the proposed method shows accuracy and robust in weather condition classification of the ABL. The current study contributes to our understanding the ABL, which is important for aviation safety, weather forecast and climate models.

Disclosures

The authors declare that there are no conflicts of interest related to this article.

References

1. J. R. Garratt, "Review: the atmospheric boundary layer," Earth-Sci. Rev. **37**(1-2), 89–134 (1994).
2. ICAO, "Manual on Low-Level Wind Shear," International Civil Aviation Organization (2005).
3. Y. Cao, Z. Wu, and Z. Xu, "Effects of rainfall on aircraft aerodynamics," Prog. Aeronaut. Sci. **71**, 85–127 (2014).
4. A. M. Weickmann, C. J. Senff, S. C. Tucker, W. A. Brewer, R. M. Banta, S. P. Sandberg, D. C. Law, and R. M. Hardesty, "Doppler Lidar Estimation of Mixing Height Using Turbulence, Shear, and Aerosol Profiles," J. Atmos. Ocean. Tech. **26**(4), 673–688 (2009).
5. B. Liu, Z. Wang, Y. Cai, P. Wechsler, W. Kuestner, M. Burkhart, and W. Welch, "Compact airborne Raman lidar for profiling aerosol, water vapor and clouds," Opt. Express **22**(17), 20613–20621 (2014).
6. J. Yang, Z. Wang, A. J. Heymsfield, and J. R. French, "Characteristics of vertical air motion in isolated convective clouds," Atmos. Chem. Phys. **16**(15), 10159–10173 (2016).
7. T. Luo, Z. Wang, D. Zhang, and B. Chen, "Marine boundary layer structure as observed by A-train satellites," Atmos. Chem. Phys. **16**(9), 5891–5903 (2016).
8. J. Li, Q. Lv, B. Jian, M. Zhang, C. Zhao, Q. Fu, K. Kawamoto, and H. Zhang, "The impact of atmospheric stability and wind shear on vertical cloud overlap over the Tibetan Plateau," Atmos. Chem. Phys. **18**(10), 7329–7343 (2018).
9. J. Lauros, E. D. Nilsson, M. Dal Maso, and M. Kulmala, "Contribution of mixing in the ABL to new particle formation based on observations," Atmos. Chem. Phys. **7**(18), 4781–4792 (2007).
10. T. Su, Z. Li, C. Li, J. Li, W. Han, C. Shen, W. Tan, J. Wei, and J. Guo, "The significant impact of aerosol vertical structure on lower atmosphere stability and its critical role in aerosol–planetary boundary layer (PBL) interactions," Atmos. Chem. Phys. **20**(6), 3713–3724 (2020).

Optics EXPRESS

11. B. Adler, K. Babić, N. Kalthoff, F. Lohou, M. Lothon, C. Dione, X. Pedruzo-Bagazgoitia, and H. Andersen, "Nocturnal low-level clouds in the atmospheric boundary layer over southern West Africa: an observation-based analysis of conditions and processes," Atmos. Chem. Phys. **19**(1), 663–681 (2019).
12. S. Teng, H. Hu, C. Liu, F. Hu, Z. Wang, and Y. Yin, "Numerical simulation of raindrop scattering for C-band dual-polarization Doppler weather radar parameters," J. Quant. Spectrosc. Radiat. Transfer **213**, 133–142 (2018).
13. R. G. Carneiro and G. Fisch, "Observational analysis of the daily cycle of the planetary boundary layer in the central Amazon during a non-El Niño year and El Niño year (GoAmazon project 2014/5)," Atmos. Chem. Phys. **20**(9), 5547–5558 (2020).
14. T. Nomokonova, K. Ebell, U. Löhnert, M. Maturilli, and C. Ritter, "The influence of water vapor anomalies on clouds and their radiative effect at Ny-Ålesund," Atmos. Chem. Phys. **20**(8), 5157–5173 (2020).
15. D. Wang, I. S. Stachlewska, J. Delanoë, D. Ene, X. Song, and D. Schüttemeyer, "Spatio-temporal discrimination of molecular, aerosol and cloud scattering and polarization using a combination of a Raman lidar, Doppler cloud radar and microwave radiometer," Opt. Express **28**(14), 20117–20134 (2020).
16. C. Wang, M. Jia, H. Xia, Y. Wu, T. Wei, X. Shang, C. Yang, X. Xue, and X. Dou, "Relationship analysis of PM2.5 and boundary layer height using an aerosol and turbulence detection lidar," Atmos. Meas. Tech. **12**(6), 3303–3315 (2019).
17. T. Su, Z. Li, and R. Kahn, "Relationships between the planetary boundary layer height and surface pollutants derived from lidar observations over China: regional pattern and influencing factors," Atmos. Chem. Phys. **18**(21), 15921–15935 (2018).
18. V. Banakh and I. Smalikho, "Lidar Studies of Wind Turbulence in the Stable Atmospheric Boundary Layer," Remote Sens. **10**(8), 1219 (2018).
19. A. J. Manninen, T. Marke, M. Tuononen, and E. J. O'Connor, "Atmospheric Boundary Layer Classification With Doppler Lidar," J. Geophys. Res.: Atmos. **123**(15), 8172–8189 (2018).
20. C. Wang, H. Xia, M. Shangguan, Y. Wu, L. Wang, L. Zhao, J. Qiu, and R. Zhang, "1.5 μm polarization coherent lidar incorporating time-division multiplexing," Opt. Express **25**(17), 20663–20674 (2017).
21. M. Aoki, H. Iwai, K. Nakagawa, S. Ishii, and K. Mizutani, "Measurements of Rainfall Velocity and Raindrop Size Distribution Using Coherent Doppler Lidar," J. Atmos. Ocean. Tech. **33**(9), 1949–1966 (2016).
22. T. Wei, H. Xia, J. Hu, C. Wang, M. Shangguan, L. Wang, M. Jia, and X. Dou, "Simultaneous wind and rainfall detection by power spectrum analysis using a VAD scanning coherent Doppler lidar," Opt. Express **27**(22), 31235–31245 (2019).
23. M. D. Shupe, "A ground-based multisensor cloud phase classifier," Geophys. Res. Lett. **34**(22), L22809 (2007).
24. V. M. Melnikov and R. J. Doviak, "Turbulence and Wind Shear in Layers of Large Doppler Spectrum Width in Stratiform Precipitation," J. Atmos. Ocean. Tech. **26**(3), 430–443 (2009).
25. P. Kollias, J. Rémillard, E. Luke, and W. Szyrmer, "Cloud radar Doppler spectra in drizzling stratiform clouds: 1. Forward modeling and remote sensing applications," J. Geophys. Res. **116**(D13), D13201 (2011).
26. F. Tridon and A. Battaglia, "Dual-frequency radar Doppler spectral retrieval of rain drop size distributions and entangled dynamics variables," J. Geophys. Res.: Atmos. **120**(11), 5585–5601 (2015).
27. A. Sathe and J. Mann, "A review of turbulence measurements using ground-based wind lidars," Atmos. Meas. Tech. **6**(11), 3147–3167 (2013).
28. T. Wei, H. Xia, Y. Wu, J. Yuan, C. Wang, and X. Dou, "Inversion probability enhancement of all-fiber CDWL by noise modeling and robust fitting," Opt. Express **28**(20), 29662–29675 (2020).
29. M. Jia, J. Yuan, C. Wang, H. Xia, Y. Wu, L. Zhao, T. Wei, J. Wu, L. Wang, S. Y. Gu, L. Liu, D. Lu, R. Chen, X. Xue, and X. Dou, "Long-lived high-frequency gravity waves in the atmospheric boundary layer: observations and simulations," Atmos. Chem. Phys. **19**(24), 15431–15446 (2019).
30. V. A. Banakh, A. Brewer, E. L. Pichugina, and I. N. Smalikho, "Measurements of wind velocity and direction with coherent Doppler lidar in conditions of a weak echo signal," Atmos. Oceanic Opt. **23**(5), 381–388 (2010).
31. Y. Pan, S. Zhang, Q. Li, L. Ma, S. Jiang, L. Lei, W. Lyu, and Z. Wang, "Analysis of convective instability data derived from a ground-based microwave radiometer before triggering operations for artificial lightning," Atmos. Res. **243**, 105005 (2020).
32. R. Frehlich, "Simulation of Coherent Doppler Lidar Performance in the Weak-Signal Regime," J. Atmos. Ocean. Tech. **13**(3), 646–658 (1996).
33. V. A. Banakh, I. N. Smalikho, and A. V. Falits, "Estimation of the turbulence energy dissipation rate in the atmospheric boundary layer from measurements of the radial wind velocity by micropulse coherent Doppler lidar," Opt. Express **25**(19), 22679–22692 (2017).
34. I. M. Brooks, "Finding Boundary Layer Top: Application of a Wavelet Covariance Transform to Lidar Backscatter Profiles," J. Atmos. Ocean. Tech. **20**(8), 1092–1105 (2003).
35. S. R. Pal, W. Steinbrecht, and A. I. Carswell, "Automated method for lidar determination of cloud-base height and vertical extent," Appl. Opt. **31**(10), 1488–1494 (1992).
36. H. Baars, A. Ansmann, R. Engelmann, and D. Althausen, "Continuous monitoring of the boundary-layer top with lidar," Atmos. Chem. Phys. **8**(23), 7281–7296 (2008).
37. M. Tuononen, E. J. O'Connor, V. A. Sinclair, and V. Vakkari, "Low-Level Jets over Utö, Finland, Based on Doppler Lidar Observations," J. Appl. Meteorol. **56**(9), 2577–2594 (2017).
38. R. B. S. Roland and B. Stull, "*An Introduction to Boundary Layer Meteorology*," Springer Netherlands (1988).

Optics EXPRESS

39. V. A. Banakh, I. N. Smalikho, A. V. Falits, B. D. Belan, M. Y. Arshinov, and P. N. Antokhin, "Joint radiosonde and doppler lidar measurements of wind in the atmospheric boundary layer," Atmos. Oceanic Opt. **28**(2), 185–191 (2015).
40. I. N. Smalikho and V. A. Banakh, "Measurements of wind turbulence parameters by a conically scanning coherent Doppler lidar in the atmospheric boundary layer," Atmos. Meas. Tech. **10**(11), 4191–4208 (2017).
41. J. Yuan and H. Xia, "A month lidar results during the experiment," figshare (2020), http://doi.org/10.6084/m9.figshare.13232615.v1.
42. V. Vakkari, E. J. Connor, A. Nisantzi, R. E. Mamouri, and D. G. Hadjimitsis, "Low-level mixing height detection in coastal locations with a scanning Doppler lidar," Atmos. Meas. Tech. **8**(4), 1875–1885 (2015).
43. B. J. Brooks, F. Davies, R. J. Hogan, C. D. Westbrook, I. M. Brooks, A. J. Illingworth, and E. J. O'Connor, "A Method for Estimating the Turbulent Kinetic Energy Dissipation Rate from a Vertically Pointing Doppler Lidar, and Independent Evaluation from Balloon-Borne In Situ Measurements," J. Atmos. Ocean. Tech. **27**(10), 1652–1664 (2010).
44. P. Borque, E. Luke, and P. Kollias, "On the unified estimation of turbulence eddy dissipation rate using Doppler cloud radars and lidars," J. Geophys. Res.: Atmos. **121**(10), 5972–5989 (2016).